

Acoustic vibrations of a silica-embedded gold nanoparticle: elastic anisotropy

Daniel B. Murray*

Department of Physics, Okanagan University College, Kelowna, British Columbia, Canada V1V 1V7

S. Dhara,[†] T. R. Ravindran, K. G. M. Nair, and S. Kalavathi

Materials Science Division, Indira Gandhi Centre for Atomic Research, Kalpakkam 603 102, India

Lucien Saviot[‡]

*Laboratoire de Réactivité des Solides, UMR 5613 CNRS - Université de Bourgogne
9 avenue A. Savary, BP 47870 - 21078 Dijon - France*

Eugène Duval

*Laboratoire de Physico-Chimie des Matériaux Luminescents, CNRS and Université Lyon I,
Bâtiment 203, 43 Boulevard du 11 Novembre 1918, 69622 Villeurbanne Cedex, France*

(Dated: September 17, 2018)

Spherical gold nanoclusters are grown by 1.8 MeV Au⁺⁺ ion implantation into an amorphous silica matrix and subsequent air annealing at 873 K. Ultraviolet and visible light absorption confirms the presence of a dipolar surface plasmon peak at the expected location for a gold sphere in silica. Grazing incidence X-ray diffraction shows peaks corresponding to fcc gold with lattice spacing close to that of bulk gold, as well as allowing estimation of cluster size using Scherrer's formula. Low frequency Raman scattering reveals a relatively narrow peak, suggesting a narrow distribution of nanocrystal diameters. Acoustic phonon frequencies corresponding to the spheroidal quadrupolar vibrations of a continuum sphere with the anisotropic elasticity of gold are calculated using a novel method of molecular dynamics and extrapolation to the continuum limit using relatively small numbers of point masses. The study confirms high energy ion implantation as a method capable of producing gold nanocrystals with spherical shape and well controlled size.

I. INTRODUCTION

A free elastic sphere has vibrational modes whose lowest frequency is on the order of the speed of sound divided by the sphere radius. This classic problem of elastic mechanics was solved by Lamb in 1882¹ for the case of a homogeneous sphere with isotropic elasticity.

Ninety years later, this solution found application in explaining anomalies of the specific heat of powders of spherical lead particles 2 to 4 nm in size.² Direct observations of vibrational modes of mixed spinel (MgCr₂O₄-MgAl₂O₄) microcrystallites 22 to 35 nm in diameter³ became possible by shining an intense laser beam onto the sample and carefully analyzing the scattered light to detect scattered frequencies slightly above and slightly below the laser frequency. The frequency shift of the light is equal to a vibrational frequency of the spinel microcrystallite. Since then, Raman and Brillouin scattering have remained powerful tools in the characterization of "nanoparticles" – particles with diameters on the order of a few to a few dozen nanometers.

The nanoparticles in these experiments are often not free, but rather embedded in solid materials such as glass. The Lamb solution does not directly apply since it assumes zero traction force boundary conditions of the sphere (*i.e.* a free surface). Initial attempts^{4,5} to generalize the calculation to an isotropic elastic continuum sphere embedded in an infinite elastic matrix are in error.⁶ But an earlier calculation⁷ in the geophysics literature had correctly solved the problem and showed that

embedded sphere vibrations can be accurately approximated with complex-valued pseudo-frequencies ω where $\text{Re}(\omega)$ is the center frequency of the Raman peak and $2\text{Im}(\omega)$ is the full width at half maximum (FWHM). Correct application of this solution to nanoparticles was made only recently.^{8,9,10}

Vibrations of an embedded sphere are described in terms of a displacement field $\vec{u}(\vec{r}, t)$ which equals $\vec{r} - \vec{R}$ where \vec{R} is the equilibrium position of a material point and \vec{r} is its displaced position. Due to the spherical symmetry, it is convenient to choose the origin at the center of the sphere and use spherical coordinates r , θ and ϕ . The time dependence is $\exp(-i\omega t)$ where ω is a complex number. In general, a vector field \vec{u} is the sum of a zero-curl field $\vec{\nabla}\Phi$ and a zero divergence field $\vec{\nabla} \times \vec{\Xi}$ where $\Phi(\vec{r})$ is a scalar field and $\vec{\Xi}(\vec{r})$ is a vector field.

In the situation of an isotropic, homogeneous elastic medium with transverse speed of sound v_T and longitudinal speed of sound v_L , normal modes are found by solving two uncoupled equations

$$(\nabla^2 + k_L^2)\Phi = 0 \quad (1)$$

and

$$(\nabla^2 + k_T^2)\vec{\Xi} = \vec{0} \quad (2)$$

where $k_L = \omega/v_L$ and $k_T = \omega/v_T$.

For convenience, the original Lamb solution will be called the Free Sphere Model (FSM). The isotropic sphere embedded in an infinite matrix will be called the Complex Frequency Model (CFM).

Whether for FSM or CFM, there are some solutions of the equation of motion with $\vec{\nabla} \cdot \vec{u} = 0$. Lamb called these the “first class” and the modern word is “torsional” (TOR). Apart from torsional modes, an important special case are radial or “breathing” modes, in which \vec{u} is purely along the r -direction and depends only on r and not on θ or ϕ . In this case \vec{u} is of the form $\vec{\nabla}\Phi$. The remaining modes of what Lamb called the “second class”, now called “spheroidal” (SPH), have a more complicated form:

$$\vec{u} = \vec{\nabla}\Phi + \vec{\nabla} \times \vec{\nabla} \times (\vec{r}\psi) \quad (3)$$

where Φ and ψ are scalar fields. Apart from the breathing modes, spheroidal modes are neither zero curl nor zero divergence.

It can be said that torsional modes are purely transverse in nature. As a result their frequencies depend only on v_T . The breathing modes are purely longitudinal, but mode frequencies depend on both v_T and v_L . The remaining spheroidal modes are a mixture of motions, but in most cases their frequencies depend primarily on v_T and only weakly on v_L , so they are predominantly transverse in character. For a generic material with Poisson ratio $\frac{1}{3}$, 80% of all modes, counting both TOR and SPH, are more transverse, while 20% are more longitudinal.

To systematically label FSM or CFM modes, it is convenient to use index $q \in \{\text{TOR, SPH}\}$. In addition, modes have an angular momentum number $\ell \in \{0, 1, 2, \dots\}$ and a z -angular momentum m where $-\ell \leq m \leq \ell$. For brevity we consider only the $m = 0$ case below. But it is important to keep in mind that FSM and CFM modes have degeneracy $2\ell + 1$. There is also a solution index $n \in \{0, 1, 2, \dots\}$. The scalar field Φ satisfying Eq. (1) has the form

$$\Phi(r, \theta) = j_\ell(k_L r) P_\ell(\cos \theta) \quad (4)$$

where j_ℓ are spherical Bessel functions and P_ℓ are Legendre polynomials. The scalar field ψ in Eq. (3) has the form

$$\psi(r, \theta) = j_\ell(k_T r) P_\ell(\cos \theta). \quad (5)$$

A given normal mode, whether FSM or CFM, will be denoted (q, ℓ, m, n) and its frequency is $\omega_{q\ell n}^{\text{FSM}}$ or $\omega_{q\ell n}^{\text{CFM}}$.

The first applications of the correct CFM solution for an isotropic continuum sphere embedded in a matrix were restricted to spheroidal modes.^{8,9} Group theoretical arguments¹¹ show that in the absence of any kind of anisotropy or non-sphericity, and in the limit that the nanoparticle is much smaller than the wavelength of the laser light, only the modes (SPH, $\ell=0$) and (SPH, $\ell=2$) can lead to Raman scattering. Correct calculations of the CFM torsional and spheroidal $\ell \neq 0$ mode frequencies were reported later.¹⁰ Even so, the usage of complex-valued frequencies of normal modes is problematic. There is no corresponding displacement field.

Clarification of the significance of CFM calculations was obtained through an exhaustive calculation of all

of the real-valued frequencies of an isotropic spherical nanoparticle embedded in a large, but finite matrix with a free spherical outer surface of radius R_m .⁶ This is called the Core-Shell Model (CSM). Taking the limit $R_m \rightarrow \infty$, the number of CSM modes in a given range of frequency becomes infinite, and has the Debye density of states. However, assuming uniform random phase excitation of the CSM modes, the mean squared displacement within the nanoparticle exhibits peaks whose positions agree closely with the real part of CFM modes, and whose FWHM agree closely with twice the imaginary parts of CFM modes. Thus, CFM calculations have a solid basis and utility, even if the corresponding CFM modes must be treated with caution.

Both FSM and CFM have limitations of applicability to real systems. (1) Nanoparticles are not truly spherical in shape, although the dynamics of most elaboration processes make them approximately that way and transmission electron microscopy (TEM) images confirm this. (2) For small nanoparticles (smaller than those in the present study), the wavelength of even the low-lying modes is not long compared to interatomic spacing, so that we are not close to the center of the Brillouin zone and the acoustic limit. (3) There will be deviations of the properties of the nanoparticle material from the same material in the bulk due to surface effects. (4) In a given sample, the radii of nanoparticles will have a distribution, rather than a single value. (5) The interface between the nanoparticle and the matrix is not always correctly described in terms of continuity of the displacement field and components of the stress tensor.¹² (6) The speed of sound within the nanoparticle depends on the direction of propagation if the elasticity of the material is anisotropic. Only the last issue is addressed in this paper.

II. ELASTIC ANISOTROPY

Since these words are frequently misused, we recall that “isotropic” means “unchanging under rotation” while “homogeneous” means “unchanging under translation”. Although bulk polycrystalline gold is elastically isotropic, a single crystal of gold is not. In fact, the noble metals (Au, Ag, Cu) are remarkably anisotropic. Depending on the direction of propagation in the crystal, a transverse acoustic (low frequency) sound wave can travel at speeds varying from 867 m/s to 1482 m/s. The longitudinal speed of sound varies less, ranging from 3147 m/s to 3440 m/s. But since all FSM and CFM modes depend on v_T , it must be expected that the strong transverse anisotropy will play an important role.

Application of FSM to elastically anisotropic crystals (in fact, no crystalline material is elastically isotropic) goes back many years. Since the theory asked for v_T and v_L , it was common to simply use the speeds of sound in the bulk polycrystalline material, sometimes with apology¹³ but usually without. One approach is to make use of the speeds of sound along the principal

crystal directions, (*e.g.* $\langle 100 \rangle$, $\langle 110 \rangle$ and $\langle 111 \rangle$ in silicon¹⁴) so as to get several different estimates of the frequencies.

The elastic mechanical problem of calculating the vibrational modes of a free sphere with anisotropic elasticity can be set up analytically for certain special kinds of anisotropy,¹⁵ but not for cubic crystalline elasticity such as that of fcc gold. Numerical techniques for finding eigenfrequencies of an object with arbitrary elasticity and a variety of special shapes have long been known.^{16,17}

Our numerical method used here varies only slightly from a previous one.¹⁰ Its features are: (1) arbitrary cubic crystalline elasticity including arbitrarily high anisotropy (unlike the earlier method¹⁰ which numerically blows up when faced with the anisotropy of a noble metal, but worked for silicon); (2) ease of handling a nanoparticle of arbitrary shape; (3) ready extendability to inhomogeneous density and elasticity; (4) generalizability (with simple modification) to hexagonal and other crystal symmetries; (4) self-diagnosis of numerical convergence; (5) rapid convergence; (6) conceptual simplicity.

Our approach can be described as a Finite Difference Time Domain (FDTD) calculation, and also as molecular dynamics (MD), the former phrase being common in the engineering literature. The continuum sphere of radius R_p and density ρ_p is approximated by N equal point masses arranged in a simple cubic (SC) lattice. The point masses do not represent atoms. For calculations reported here, N was as high as 8000. The use of an SC lattice is associated with the cubic symmetry of the elasticity but does not preclude simulations of objects of crystalline material with fcc, bcc or diamond structures, as well as isotropic solids such as glass. The method as detailed here applies only to the homogeneous cubic case. The method is unrelated to calculations which model the microscopic inter-atomic forces such as the Tersoff potential for silicon or the Keating model. Rather, it is a continuum model of the material, involving only the bulk elastic constants and the density.

III. MOLECULAR DYNAMICS METHOD

Our method is a molecular dynamics calculation. While this approach can readily be extended to the more general case of an object of arbitrary shape with inhomogeneous anisotropic elasticity, we choose for brevity only to present the case of a spherical object with cubic crystalline elasticity. A simple cubic lattice with lattice parameter a of N identical point particles of mass ρa^3 interacting through “springs” has particle positions \vec{r}_j integrated in time and Fourier transformed in order to obtain mode frequencies. Each particle has six first neighbors, twelve second neighbours, eight third neighbors and so on. Every pair (i, j) of first neighbors are coupled by potential energy $\frac{1}{2}k_{sp1}(\|\vec{r}_i - \vec{r}_j\| - a)^2$. Second neighbor pairs (i, j) are coupled by $\frac{1}{2}k_{sp2}(\|\vec{r}_i - \vec{r}_j\| - \sqrt{2}a)^2$. Third neigh-

bor pairs (i, j) are coupled by $\frac{1}{2}k_{sp3}(\|\vec{r}_i - \vec{r}_j\| - \sqrt{3}a)^2$. Fourth neighbor pairs (i, j) are coupled by $\frac{1}{2}k_{sp4}(\|\vec{r}_i - \vec{r}_j\| - \sqrt{4}a)^2$. Fifth neighbor pairs (i, j) are coupled by $\frac{1}{2}k_{sp5}(\|\vec{r}_i - \vec{r}_j\| - \sqrt{5}a)^2$. Pairs are not double counted. Cubic octets are coupled by $(k_{8pt}/4a^2)(D - 6a^2)^2$ where $D = \sum_{j=1}^8 \|\vec{R}_{cm} - \vec{r}_j\|^2$ and $\vec{R}_{cm} = \frac{1}{8} \sum_{j=1}^8 \vec{r}_j$.

No microscopic physical interpretation is offered for the k_{8pt} term. Its purpose is to allow reproduction of the bulk elastic constants rather than to represent the potentials due to atomic bonding among atoms. It is possible to approximate interatomic interactions among atoms in certain special kinds of crystals using model potentials.^{18,19,20} Our approach is not limited to certain kinds of crystals, but rather to continuum materials with completely general cubic elasticity. For this purpose, it is numerically more efficient to use the potentials that we employ.

Although we have introduced six force constants, (k_{sp1} , k_{sp2} , k_{sp3} , k_{sp4} , k_{sp5} , and k_{8pt}) only k_{sp1} , k_{sp3} , and k_{8pt} are used for the numerical calculations of this paper. A previous paper¹⁰ used k_{sp1} , k_{sp2} , and k_{8pt} , but was limited to materials of lower elastic anisotropy as will be explained below. It is advantageous to use the earlier method for less isotropic materials since numerical convergence is faster as N increases.

The next step is to show how the force constants are related to the bulk elastic constants of the material of the nanosphere. A cubic crystal (in particular, any material with bcc, fcc, diamond or zincblende crystal structure) has three elastic constants: C_{11} , C_{12} , and C_{44} . For an isotropic material, $C_{12} = C_{11} - 2C_{44}$. The degree of elastic anisotropy is quantified by the Zener anisotropy ratio, A_Z , where

$$A_Z = \frac{2C_{44}}{C_{11} - C_{12}} \quad (6)$$

Elastic isotropy corresponds to $A_Z = 1$, and anisotropic materials can have A_Z above or below 1. The Zener anisotropy of gold is 2.92. Silver and copper have comparable anisotropies.

The bulk modulus of an arbitrary cubic elastic material is $B = (C_{11} + 2C_{12})/3$. Let V denote volume. A small isotropic dilatation $\delta = dV/V$ stretches all neighbor distances proportionally and leads to stored energy $\frac{1}{2}VB\delta^2$, so that we obtain

$$a(C_{11} + 2C_{12}) = k_{sp1} + 4k_{sp2} + 4k_{sp3} + 4k_{sp4} + 20k_{sp5} + 24k_{8pt} \quad (7)$$

Considering that a longitudinal plane wave moves along the x -axis at speed $\sqrt{C_{11}/\rho}$, we find

$$aC_{11} = k_{sp1} + 2k_{sp2} + \frac{4}{3}k_{sp3} + 4k_{sp4} + 13.6k_{sp5} + 8k_{8pt} \quad (8)$$

Finally, considering that a transverse plane wave moves along the x -axis at speed $\sqrt{C_{44}/\rho}$, we find

$$aC_{44} = k_{sp2} + \frac{4}{3}k_{sp3} + 3.2k_{sp5} \quad (9)$$

By subtracting Eq. 8 from Eq. 7, we obtain

$$aC_{12} = k_{sp2} + \frac{4}{3}k_{sp3} + 3.2k_{sp5} + 8k_{8pt} \quad (10)$$

Note that if $k_{8pt} = 0$, C_{12} and C_{44} are exactly the same. This has been numerically verified up to tenth neighbours. It is coincidentally the case that C_{12} and C_{44} are almost the same for NaCl, so the elastic properties of NaCl could be modelled without the k_{8pt} term. In addition, C_{12} and C_{44} are equal for isotropic materials with Poisson ratio $\frac{1}{4}$, such as polycrystalline Cerium, once again allowing modelling with two-body forces alone.

For other materials, it is essential to include an interaction apart from two-particle forces. This is the reason for including the k_{8pt} potential term. Eight masses must be involved in order to have a term that in itself respects cubic symmetry. However, it would also be workable though not obviously advantageous to have used a three body interaction term.

Three interaction terms, including k_{8pt} , must be used to exactly fit the three elastic parameters C_{11} , C_{12} , and C_{44} . If, as in earlier work¹⁰, only k_{sp1} , k_{sp2} , and k_{8pt} are used, then

$$k_{sp1} = a(C_{11} - (C_{12} + C_{44})), \quad (11)$$

Note that materials with Zener anisotropy above 2 will have negative k_{sp1} . This leads to instability of molecular dynamics simulations of the lattice.

Another option is to use only k_{sp1} , k_{sp3} , and k_{8pt} . Inversion allows the three force constants to be obtained for a general cubically elastic material:

$$k_{sp1} = a(C_{11} - C_{12}), \quad (12)$$

$$k_{sp3} = \frac{3a}{4}C_{44} \quad (13)$$

and

$$k_{8pt} = \frac{1}{8}a(C_{12} - C_{44}). \quad (14)$$

Note that k_{sp1} and k_{sp3} are never negative. It can be the case that k_{8pt} is negative for some materials, but in practice this does not lead to instability of the molecular dynamics simulations. As a result, any cubic material can be simulated.

The frequency dependence of a given mode is $f(N)$. A sequence of simulations with N varying from a few hundred to 8000 is used to extrapolate $f(\infty)$, which is the continuum limit. Accurate results are obtainable with just a few thousand.

The correctness and degree of convergence of our MD method was checked by comparing its results to those of the Lamb solution for isotropic elastic materials of various Poisson ratios. The results of the two methods agree closely.

TABLE I: Frequencies of selected vibrational modes of an elastic continuum sphere with the elastic constants of single crystal gold of radius R are shown. The value given is ωR (in m/s) where ω is the frequency in radians per second and R is the nanosphere radius in metres.

q	ℓ	n	ωR	degeneracy	symmetry
SPH	2	0	2342	3	T_{2g}
SPH	2	0	3779	2	E_g
SPH	0	0	10315	1	A_{1g}

IV. MOLECULAR DYNAMICS RESULTS

A sequence of simulations with increasing N is performed in order to extrapolate the limit of infinite N . The purpose of the calculation is to solve for the vibrational frequencies of a continuum elastic sphere, and does not take into account the crystal structure of the material or dispersion (frequency dependence of sound speed) of phonons.

The time duration of the simulation is determined by the frequency resolution that is desired. The initial velocity distribution corresponds to an FSM mode. The z -axis of the desired FSM mode is randomly oriented for each run relative to the axis of the cubic lattice.

A Fourier transform is carried out of the motion of several randomly selected mass points along various axes. A plot is then made of the power spectrum versus $1/N$. This permits extrapolation of the frequency of each mode to infinite N . The extrapolation is done visually.

The elastic constants used²¹ for monocrystalline fcc gold at 300 K were $C_{11} = 191$ GPa, $C_{12} = 162$ GPa, $C_{44} = 42.4$ GPa, and $\rho = 19.283$ g/cc.

Table I shows results of the molecular dynamics simulations. Frequencies are presented in terms of the ratio ωR . For an isotropic material, it is beneficial to use dimensionless frequencies such as $\eta = \omega R/v_T$ and $\xi = \omega R/v_L$. In this problem, the anisotropy of the elasticity means that there is no convenient sound speed scale to form a dimensionless frequency. However, expressing results in terms of ωR exploits the scale invariance of the problem as long as continuum elasticity is assumed.

The frequencies in Tab. I are classified according to the symmetry of the initial disturbance used to excite them. In each case, velocity fields of spheroidal FSM modes of angular momentum ℓ are used as the initial disturbance. The z -axis of the velocity field is randomized with respect to the axes of the lattice for each run. The mode degeneracies in Tab. I were found by gradually distorting the shape of the sphere so as to break all symmetry, and noting into how many frequencies each mode splits. The $\ell=0$ spheroidal mode frequency is calculated, but the Raman scattering strength is typically much smaller than for the $\ell=2$ spheroidal mode.

It would be expected on the basis of group theoretical considerations that a 5-fold degenerate (SPH,2) mode of an isotropic sphere would be broken into two different levels by lowering the elastic symmetry to that of a cu-

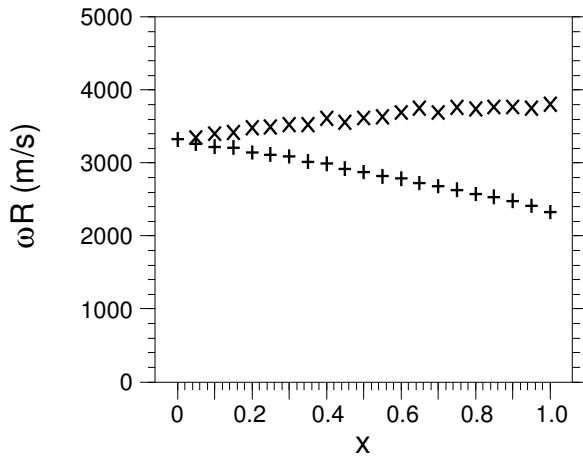


FIG. 1: Perturbed frequencies of the initially fivefold degenerate quadrupolar spheroidal modes of a free sphere are shown as the parameter x is varied. $x = 0$ corresponds to directionally averaged isotropic gold while $x = 1$ corresponds to true anisotropic gold. The upper and lower branches are twofold and threefold degenerate respectively.

bic crystal. The corresponding representations are E_g with two dimensions and T_{2g} with three dimensions.²² To illustrate this, Fig. 1 shows how the frequencies vary as the amount of anisotropy is continuously varied. Let C_{11a} , C_{12a} , and C_{44a} be the elastic constants of directionally averaged gold. These are based on the directionally averaged sound speeds of 3330 m/s and 1250 m/s. In particular, $C_{11a} = (3330 \text{ m/s})(3330 \text{ m/s})(19293 \text{ kg/m}^3)$ and $C_{44a} = (1250 \text{ m/s})(1250 \text{ m/s})(19293 \text{ kg/m}^3)$. Also, since isotropy is assumed, $C_{12a} = C_{11a} - 2C_{44a}$. The elastic constants of true monocrystalline bulk gold are C_{11b} , C_{12b} , and C_{44b} as given earlier in this section. The frequencies in Fig. 1 are done with elastic constants $C_{ij} = xC_{ija} + (1-x)C_{ijb}$. Note how the isotropic (SPH,2) mode at $\omega R = 3320 \text{ m/s}$ continuously splits into two modes.

V. MATRIX EFFECT

The molecular dynamics calculation results shown in Tab. I assume a gold sphere with a free surface. However the gold nanospheres reported in the experimental results of this paper are embedded in amorphous silica. As a result, the outer surface of the gold spheres is not free. The silica will affect the vibrational frequencies.

The complex frequency model (CFM)^{6,7,9,10} calculates the complex-valued vibrational frequencies of a sphere embedded in an infinite matrix. Both the sphere and the matrix are assumed to be continuous, homogeneous and isotropic. Since vibrational modes of the gold sphere are damped by the propagation of sound waves into the matrix, the modes have complex valued frequencies. The imaginary part of the frequency is related to the damping time of the mode.

To treat gold as an isotropic material requires an ap-

TABLE II: FSM and CFM frequencies for a directionally averaged (elastically isotropic) sphere of gold. For the complex CFM frequencies, the gold sphere is embedded in a silica matrix. The value given is ωR where ω is the frequency in radians per second and R is the sphere radius in metres.

q	ℓ	n	FSM ωR	$Re(\omega R)$	$Im(\omega R)$	degeneracy
SPH	2	0	3320	4261	322	5
SPH	0	0	9789	10185	542	1

proximation to be made about its elastic properties. We use directionally averaged speeds of sound. The longitudinal and transverse speeds are separately averaged. The results are 1250 m/s and 3330 m/s.

Amorphous silica is an isotropic material. We assume speeds of sound of 3760 m/s and 5950 m/s and a density of 2.20 g/cc.

Results of CFM calculations are shown in Tab. II. FSM calculations based on Lamb's 1882 solution for a free sphere are also given.

We can either model the anisotropic elasticity of gold using molecular dynamics calculations for a free sphere or else model the effects of the silica matrix using CFM for an isotropic sphere. We have no way to simultaneously model both anisotropy and matrix effects.

In Tab. II, note that the damping of the modes is relatively small, based on the low imaginary parts of the CFM frequencies. However, the (SPH, $\ell=2$) mode is significantly upshifted by the silica matrix. This is caused by the action of the matrix to provide a spring-like reaction force acting at the outer surface of the gold sphere.²³ As a result, the MD calculations which ignore the matrix effect will require some correction.

VI. TANDETRON ACCELERATOR

Gold ion implantation was done using a 1.7 MV Tandetron accelerator (Model 4117HC) from High Voltage Engineering Europa, Amersfoort, the Netherlands. This accelerator has the "tandem" configuration where negative ions generated by a cesium sputter gold ion source are first accelerated from ground to the high voltage terminal and there the negative gold ions are converted to positive gold ions, while passing through a stripper canal filled with nitrogen gas. The same high voltage again accelerates the positive Au^{++} ions to ground potential. In this way, Au^{++} ions could be generated with energies up to 5.1 MeV with the Tandetron.

VII. SAMPLE PREPARATION

Using the Tandetron ion accelerator, Au clusters were grown by direct Au-implantation on fused quartz (amorphous silica) substrates. Implantation was performed using 1.8 MeV Au^{++} at $1 \times 10^{-5} \text{ Pa}$ with a beam current of $\approx 12 \text{ mA m}^{-2}$ to avoid substantial beam heating in

the ion fluence range of $2 \times 10^{20} - 1 \times 10^{21} \text{ m}^{-2}$. During implantation the substrate was at room temperature. The diameter of the ion beam is 1 cm, so that the total beam current is approximately $1 \mu\text{A}$. At this energy, the average penetration depth of the Au^{++} in the silica is 445.6 nm before they come to rest, with a straggling (distribution width) of 55.4 nm.²⁴ The advantage of using such a high beam energy is that structure can be created at a much greater depth below the surface of the silica substrate. High temperature air annealing at 873 K for 1 hour was performed to promote growth of the clusters as gold atoms become mobile in the silica substrate and are able to conglomerate into bulk gold metal as opposed to isolated gold atoms.

Our study emphasizes acoustic phonons of the implanted nanospheres and therefore benefits from a narrow size distribution. The 1.8 MeV beam energy is not thought to play a role apart from controlling the implantation depth of the ions. Ion implantation often results in wide size distributions.^{25,26} Implantation temperature²⁷ and post-implantation annealing²⁸ are known to play an important role in controlling average particle size and size distribution. The current density of the ion beam affects average size and size distribution when implanting silica with Ag²⁹ and Cu³⁰ and is expected from simulations²⁷ to play a similar role for gold. Laser pulse annealing³¹ is also known to be able to narrow the size distribution.

VIII. SAMPLE CHARACTERIZATION

Optical absorption spectra were recorded at room temperature in the range of 200 – 1100 nm using a Hewlett-Packard diode-array UV-visible (UV-Vis) spectrophotometer (Model 8453) with necessary signal correction for the substrate. Figure 2 shows broad peak structure corresponding to the frequency of the dipolar surface plasmon resonance of a gold sphere in a silica matrix. This is evidence of the shape of the nanoparticles being approximately spherical. The surface plasmon resonance of an ellipsoidal sphere would split into higher and lower frequencies.

Grazing incident X-ray diffraction (GIXRD) was done using Cu $K\alpha$ X-rays (wavelength = 0.15406 nm), as shown in Fig. 3. Both the (111) and (200) peaks were observed, with (111) being the stronger feature. The location of the (111) peak closely matches that expected based on a fcc unit cell size of 0.40786 nm for gold at room temperature. This was done in 0.05 degree steps with 25 s accumulation time per data point. This is an Ω - 2θ scan. Ω is 0.8 degrees. In other words, the incident X-rays enter the sample at 89.2 degrees from normal incidence.

X-ray diffraction is an indication of the crystalline domain size rather than the size of the nanosphere. However since annealing at 873 K was done, it is expected that the nanosphere would consist of a single crystal domain, and the size from GIXRD is interpreted as the size

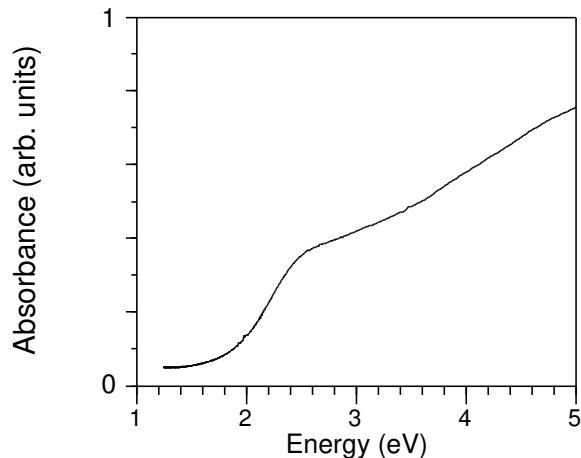


FIG. 2: Light absorbance as a function of photon energy is shown for post-annealed Au nanoclusters in silica matrix grown at fluence $1 \times 10^{21} \text{ m}^{-2}$. Structure around 2.4 eV is attributed to the dipolar surface plasmon resonance of a gold sphere embedded in silica.

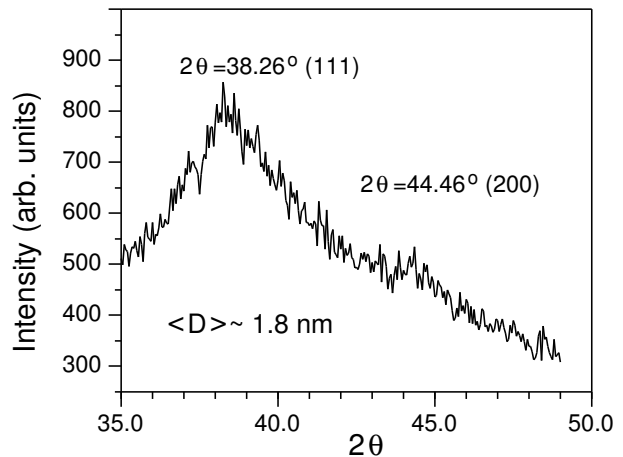


FIG. 3: Grazing incidence X-ray diffraction data is shown for gold nanospheres embedded in silica, using copper alpha X-rays. Two expected peak positions are indicated based on the fcc structure and 0.40786 nm lattice constant of bulk gold. The indicated averaged diameter estimated is based on Scherrer's formula applied to the (111) peak.

of the nanosphere.

Low-frequency Raman scattering studies were done at room temperature in the back scattering geometry, using vertically polarized 488 nm line of an argon ion laser (Coherent, USA) with 200 mW power. Unpolarized scattered light from the sample was dispersed using a double monochromator (Spex, model 14018) with instrument resolution of 1.4 cm^{-1} and detected using a cooled photomultiplier tube (FW ITT 130) operated in the photon counting mode. See Fig. 4.

A strong and relatively narrow Raman peak is seen in Fig. 4 with its peak at 22 cm^{-1} . The full width at half maximum (FWHM) of this peak is approximately

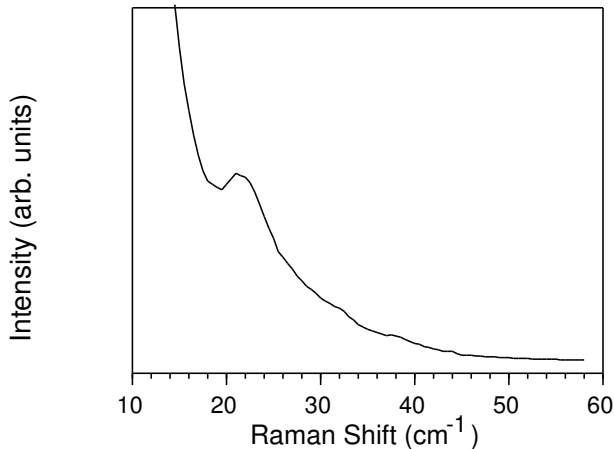


FIG. 4: Room temperature low-frequency Raman spectra for post-annealed Au nanoclusters in a silica matrix. The 4 cm^{-1} wide peak at 22 cm^{-1} is attributed to thermal spheroidal quadrupolar vibrations of the gold sphere. The broadening of the peak may be primarily due to damping of the vibration due to mechanical contact with the silica matrix.

4 cm^{-1} . This is relatively narrow compared to Raman peaks seen in other systems of embedded nanoparticles. The center of the Raman peak corresponds to an angular frequency $\omega = 4.15 \times 10^{12} \text{ rad/s}$.

IX. DISCUSSION

The low frequency Raman spectrum of our sample in Fig. 4 showed a prominent peak with an angular frequency of $4.15 \times 10^{12} \text{ rad/s}$. The average radius of the particles, as estimated from GIXRD in Fig. 3 using Scherrer's formula was 0.90 nm . The resulting experimental value of ωR is 3732 m/s .

The existence of a vibrational mode does not mean that it will appear in a Raman spectrum. For an isotropic sphere, only the (SPH,0) and (SPH,2) modes can be Raman active based on group theoretical considerations¹¹ and in practice the intensity of the (SPH,0) is much smaller. More detailed analysis, not presented here, is necessary to predict the relative Raman activity of the two different frequencies into which the (SPH,2) mode has been split by elastic anisotropy.^{22,32}

It is expected that one of the two modes with $\omega R = 2342 \text{ m/s}$ and 3779 m/s as shown in Tab. I will be the dominant feature in the Raman spectrum, but these values from MD omit the matrix effect. To estimate the effect of the matrix, we rely on comparison of FSM and CFM results in Tab. II, which shows that the matrix effect increases the frequency of the (SPH, $\ell=2$) mode by a factor of 1.28. Applying this to the MD results, the two expected locations of Raman peaks are $\omega R = 3006 \text{ m/s}$ and 4837 m/s . One is 20% lower than the location of the

experimental Raman peak while the other is 30% higher.

Based on the cubic symmetry, for modes with T_{2g} symmetry, the Raman tensor is off-diagonal while for modes with E_g symmetry, the Raman tensor is diagonal.²² In other words, T_{2g} modes will only contribute to the depolarized (VH) portion of the Raman spectrum while E_g modes only contribute to the polarized (VV) part. The Raman spectrum in our measurements is polarized. Thus, ωR is experimentally 3732 m/s and theoretically 4837 m/s .

A possible resolution of this poor agreement is that the gold nanoparticles are loosely attached to the silica matrix. In that case, FSM frequencies from Tab. I would be appropriate. Since the E_g mode frequency is 3779 , the agreement with the experimental value of 3732 m/s is compelling. Furthermore, the next paragraphs show an independent reason to believe this.

CFM calculations of the width of the peak show that it should be quite narrow. Based on the CFM value of ωR of the (SPH,2) mode given in Tab. II, the expected FWHM width of a Raman peak at 22 cm^{-1} would be 3.3 cm^{-1} , which is only slightly smaller than the observed FWHM width in Fig. 4 of 4 cm^{-1} . The increased peak width can be attributed to size variation of the gold nanoparticles within the sample as well as instrumental broadening. It is plausible to assume that the Raman width due to particle size variation, the Raman width due to mode damping, and the Raman instrumental width (1.4 cm^{-1}) combine squarewise to give the width of the observed Raman spectrum. In that case, the Raman peak FWHM width due to particle size variation is just 1.8 cm^{-1} , since $4^2 - 3.3^2 - 1.4^2 = 1.8^2$. We assume the distribution of particle radius is Gaussian with one standard deviation σ and mean R_{avg} . The FWHM of a Gaussian distribution is $2\sqrt{2 \ln 2} \sigma$. Thus, the rms variation of particle radius is estimated to be $\sigma = 0.034 R_{avg}$.

It is difficult to believe that the particle radius variation in our sample is really so small, particularly since ion implantation experiments have never given such a tight size distribution. An alternative is that CFM overestimates the true broadening due to damping. If the interface between the gold and the silica is not a tight bond then the broadening effect of the silica matrix is reduced based on a model of the interface as a thin soft layer.²³ Since gold does not readily form chemical bonds with silicon or oxygen the adhesion between the gold and silica is likely of Van der Waals type.

Acknowledgements: The authors would like to thank P. Ramamurthy of the National Centre for Ultrafast Processes, University of Madras, India for his co-operation in UV-Vis study. We thank V. S. Sastry and B. K. Panigrahi of MSD, IGCAR for their contributions in structural and implantation studies, respectively. We also thank B. Viswanathan of MSD, IGCAR for his encouragement in pursuing this work.

-
- * Electronic address: dmurray@ouc.bc.ca
† Electronic address: dhara@igcar.ernet.in
‡ Electronic address: Lucien.Saviot@u-bourgogne.fr
- ¹ H. Lamb, Proc. London Math. Soc. **13**, 189 (1881-1882).
 - ² V. Novotny, P. P. M. Meincke, and J. H. P. Watson, Phys. Rev. Lett. **28**, 901 (1972).
 - ³ E. Duval, A. Boukenter, and B. Champagnon, Phys. Rev. Lett. **56**, 2052 (1986).
 - ⁴ A. Tamura, K. Higeta, and T. Ichinokawa, J. Phys. C **15**, 4975 (1982).
 - ⁵ N. N. Ovsiyuk and V. N. Novikov, Phys. Rev. B **53**, 3113 (1996).
 - ⁶ D. B. Murray and L. Saviot, Phys. Rev. B **69**, 094305 (2004).
 - ⁷ V. Dubrovskiy and V. Morozhnik, Izv., Acad. Sci., USSR, Phys. Solid Earth **17**, 494 (1981).
 - ⁸ N. Del Fatti, C. Voisin, F. Chevy, F. Vallée, and C. Flytzanis, J. Chem. Phys. **110**, 11484 (1999).
 - ⁹ P. Verma, W. Cordts, G. Irmer, and J. Monecke, Phys. Rev. B **60**, 5778 (1999).
 - ¹⁰ L. Saviot, D. B. Murray, and M. del C. Marco de Lucas, Phys. Rev. B **69**, 113402 (2004).
 - ¹¹ E. Duval, Phys. Rev. B **46**, 5795 (1992).
 - ¹² C. W. Bettenhausen, W. C. Bowie, and M. R. Geller, Phys. Rev. B **68**, 035431 (2003).
 - ¹³ M. Fujii, T. Nagareda, S. Hayashi, and K. Yamamoto, Phys. Rev. B **44**, 6243 (1991).
 - ¹⁴ M. Fujii, Y. Kanzawa, S. Hayashi, and K. Yamamoto, Phys. Rev. B **54**, R8373 (1996).
 - ¹⁵ W. Q. Chen, J. B. Cai, G. R. Ye, and H. J. Ding, ASME J. Appl. Mech. **67**, 422 (2000).
 - ¹⁶ H. H. Demarest, J. Acoust. Soc. Am. **49**, 768 (1971).
 - ¹⁷ W. M. Visscher, A. Migliori, T. M. Bell, and R. A. Reinert, J. Acoust. Soc. Am. **90**, 2154 (1991).
 - ¹⁸ N. C. Keating, Phys. Rev. **145**, 637 (1966).
 - ¹⁹ F. H. Stillinger and T. A. Weber, Phys. Rev. B **31**, 5262 (1985).
 - ²⁰ J. Tersoff, Phys. Rev. B **39**, 5566 (1989).
 - ²¹ R. F. S. Hearmon, in *The elastic constants of crystals and other anisotropic materials*, edited by K. H. Hellwege and A. M. Hellwege (Springer-Verlag, Berlin, 1984), no. III/18 in Landolt-Börnstein Tables, pp. 1–154.
 - ²² W. Cheng and S.-F. Ren, Phys. Rev. B **65**, 205305 (2002).
 - ²³ L. Saviot and D. B. Murray, Phys. Rev. Lett. **??**, ??? (2004), accepted; cond-mat/0401579.
 - ²⁴ J. F. Ziegler, J. P. Biersack, and U. Littmark, *The Stopping and Range of Ions in Solids* (Pergamon, New York, 1985), www.srim.org.
 - ²⁵ A. Miotello, G. D. Marchi, G. Mattei, P. Mazzoldi, and C. Sada, Phys. Rev. B **63**, 075409 (2001).
 - ²⁶ V. Bandourko, N. Umeda, T. Suga, C. G. Lee, K. Kono, Y. Takeda, and N. Kishimoto, Nucl. Instr. and Meth. Phys. Res. B **206**, 606 (2003).
 - ²⁷ M. Strobel, K.-H. Heinig, W. Möller, A. Meldrum, D. S. Zhou, C. W. White, and R. A. Zuhr, Nuc. Instr. Meth. Phys. Res. B **147**, 343 (1999).
 - ²⁸ K. Fukumi, A. Chayahara, K. Kadono, T. Sakaguchi, Y. Horino, M. Miya, K. Fujii, J. Hayakawa, and M. Satou, J. Appl. Phys. **75**, 3075 (1994).
 - ²⁹ M. Dubiel, H. Hofmeister, G. L. Tan, K.-D. Schicke, and E. Wendler, Eur. Phys. J. D **24**, 361 (2003).
 - ³⁰ R. H. Magruder III, R. F. Haglund Jr., L. Yang, J. E. Wittig, and R. A. Zuhr, J. Appl. Phys. **76**, 708 (1994).
 - ³¹ R. A. Wood, P. D. Townsend, N. D. Skelland, D. E. Hole, and J. Barton, J. Appl. Phys. **74**, 5754 (1993).
 - ³² G. Bachelier and A. Mlayah, Phys. Rev. B **69**, 205408 (2004).